

Accepted Manuscript

In-situ X-ray microtomography characterization of damage in SiC_p/SiC mini-composites

C. Chateau, L. Gélébart, M. Bornert, J. Crépin, E. Boller, C. Sauder, W. Ludwig

PII: S0266-3538(11)00075-3
DOI: [10.1016/j.compscitech.2011.02.008](https://doi.org/10.1016/j.compscitech.2011.02.008)
Reference: CSTE 4933

To appear in: *Composites Science and Technology*

Received Date: 19 November 2010
Revised Date: 16 February 2011
Accepted Date: 20 February 2011



Please cite this article as: Chateau, C., Gélébart, L., Bornert, M., Crépin, J., Boller, E., Sauder, C., Ludwig, W., In-situ X-ray microtomography characterization of damage in SiC_p/SiC minicomposites, *Composites Science and Technology* (2011), doi: [10.1016/j.compscitech.2011.02.008](https://doi.org/10.1016/j.compscitech.2011.02.008)

This is a PDF file of an unedited manuscript that has been accepted for publication. As a service to our customers we are providing this early version of the manuscript. The manuscript will undergo copyediting, typesetting, and review of the resulting proof before it is published in its final form. Please note that during the production process errors may be discovered which could affect the content, and all legal disclaimers that apply to the journal pertain.

In-situ X-ray microtomography characterization of damage in SiC_f/SiC minicomposites

C.Chateau^a, L.Gélébart^{a*}, M.Bornert^{b,c}, J.Crépin^d, E.Boller^e, C.Sauder^a, W.Ludwig^f

^a CEA, DEN, SRMA, 91191 Gif-sur-Yvette, France

^b Université Paris Est, Laboratoire Navier, Ecole des Ponts ParisTech, 77455 Marne-la-Vallée Cedex, France

^c Solid Mechanics Laboratory, Ecole polytechnique, CNRS UMR 7649, 91128 Palaiseau Cedex, France

^d Centre des matériaux, Mines ParisTech, CNRS UMR 7633, BP 87, F-91003 Evry Cedex, France

^e European Synchrotron Radiation Facility, 6 rue Jules Horowitz, 38043 Grenoble Cedex, France

^f MATEIS, Université de Lyon, INSA Lyon, CNRS UMR 5510, 69621 Villeurbanne Cedex, France

* Corresponding author: lionel.gelebart@cea.fr, tel: +33169081678, fax: +33169087167

Abstract

The purpose of the present study is to characterize matrix crack propagation and fiber breaking occurrences within SiC/SiC minicomposite in order to validate later on a multiscale damage model at the local scale. An in-situ X-ray microtomography tensile test was performed at the European Synchrotron Radiation Facility (ESRF, ID19 beamline) in order to obtain 3-dimensional (3D) images at six successive loading levels. Results reveal a slow and discontinuous propagation of matrix cracks, even after the occurrence of matrix crack saturation. A few fiber failures were also observed. However, radiographs of the whole length (14 mm) of the minicomposites under a load and after the failure were more appropriate to get statistical data about fiber breaking. Thus, observations before the ultimate failure revealed only a few fibers breaking homogeneously along the minicomposite. In addition, an increase in fiber breaking density in the vicinity of the fatal matrix crack was observed after failure. These

experimental results are discussed in regards to assumptions used in usual 1-dimensional (1D) models for minicomposites.

Keywords

A. Ceramic-matrix composites (CMCs), B. Matrix cracking, C. Damage mechanics, D. X-ray computed microtomography (μ -CT).

Introduction

SiCf/SiC composites are prospective candidates for functional uses in future nuclear reactors - such as gas cooled fast reactors (GFR) - because of their favorable mechanical properties at high temperatures and after irradiation. The composites under investigation are made from a 2D fibrous preform composed of the new near-stoichiometric SiC fibers (Hi-Nicalon type S or Tyranno SA3 fibers), using the Chemical Vapor Infiltration (CVI) process. The material exhibits a nonlinear behavior due to the accumulated damage occurring between and inside the woven tows, such as through matrix cracking, fiber/matrix debonding as well as fiber breaking. Thus, a characterization of damage mechanisms within the tow is required to build and validate at local scale a multiscale predictive model. Due to their simple geometry, minicomposites (unidirectional composites containing a single bundle of fibers) are well suited to study these mechanisms. They are also frequently used to optimize the fiber/matrix interphase which dictates the matrix crack deflection along the fibers and consequently the nonlinear behavior of the composite [1, 2, 3].

Several 1D statistical models of the evolutionary damage have previously been reported [4, 5, 6, 7, 8, 9, 10, 11]. They are based on matrix and fiber failure probability laws (such as the Weibull law) and are complemented by a stress redistribution assumption in the vicinity of matrix cracks. These models may lead to satisfactory predictions of the

macroscopic response. However, microscopic phenomena cannot be fully validated because of the lack of experimental damage characterization. In fact, if the qualitative damage evolution is accepted, then observations reported in other literature were limited to the sample surface and were mostly collected after the ultimate failure [1, 6, 12, 13]. The purpose of this article is to present an experimental characterization of damage in SiCf/SiC minicomposites under a tensile load using X-ray microtomography. As reviewed by Stock [14], microtomography has been successfully used in material research. In particular, it has been used to study damage or fatigue cracks [15] in several materials such as fiber reinforced metal [16, 17, 18] or polymer [19, 20, 21] matrix composites, aluminium alloys [22, 23] or polymers (PMMA) [24]. However, tomography applied to SiCf/SiC composites has been limited to porosity observations [25, 26, 27], crack observations requiring a very high resolution because openings are smaller than 1 μm . In order to investigate matrix crack propagation through SiCf/SiC minicomposite sections, 3D images of a minicomposite under several tensile loading levels were acquired using the X-ray synchrotron source provided by the European Synchrotron Radiation Facility (ESRF). These images, reconstructed from a large number of radiographs, have been analyzed to detect matrix cracks within a small volume. Therefore, the morphology and kinetics of crack propagation through the minicomposite section can be described. In order to get statistical data on the fiber failure locations, fiber breaking has also been directly observed using a single radiograph of the entire sample. This was done for a single tensile loading level (about 80 % of the stress to failure) and after failure.

1. Material and methods

1.1. Minicomposites

The studied minicomposites were made [3] from a fibrous yarn constructed from 500 Hi-Nicalon type S fibers, with an average diameter of 13 μm . The 100 nm interphase (pyrocarbon) and the SiC matrix were deposited on the fibers using the CVI process.

The residual porosity due to the CVI process, and fiber fractions were estimated at 0.12 (± 0.04) and 0.58 (± 0.09) from polished cross-section pictures (figure 1a).

Like the woven composite, minicomposites have an elastic, damageable behavior. Their macroscopic behavior (figure 2) follows typical successive steps in accordance with damage evolution [3, 12]. The first one is an elastic domain of the minicomposite behavior: no cracking occurs. A second nonlinear step is associated with the matrix cracking (figure 1b) until saturation of crack number density (reached for a total strain of about 0.3%). A second linear domain associated with the additional elastic deformation of fibers is then observed after matrix crack saturation. The final step is characterized by a slight nonlinearity associated with fiber breaking just before the ultimate failure (close to $\approx 0.7\%$).

1.2. *Experimental procedure*

The in-situ microtomography tensile test was carried out on the ID19 beamline at the ESRF, in Grenoble, France. A specific in-situ tensile testing machine dedicated to ID19 was used to manually load the specimen (called specimen #1). The minicomposite was glued onto aluminium tabs and had a gauge length of 14 mm. Only the load was monitored using a 500 N load cell. The test was interrupted at six successive loading levels (50, 68, 74, 86, and 92 N) to record the tomography images. The corresponding load levels are reported on the typical load-strain curve presented in figure 2, and were obtained from another sample of the same batch with a classical macroscopic device.

Microtomography consists in recording a set of radiographs acquired at high resolution and at various angular positions of the sample with respect to the X-ray beam [28].

Appropriate algorithms are then used to reconstruct the 3D image from this set of radiographs. A high resolution was necessary to observe both cracks and the microstructure of the tow. Such a resolution with moderate acquisition times could only be reached through a synchrotron radiation, which gives a monochromatic, parallel and high intensity beam. The highest resolution provided on the ID19 beamline at the ESRF is a voxel (volumetric pixel) size of 0.28 μm , identical in all three directions. To observe a 1.65 mm total length, three acquisitions at three successive axial positions were required. In addition, these acquisitions, or scans, were performed at four distinct distances (8, 14, 26 and 36 mm) from the sample to the camera (a Fast Readout Low Noise – FreLoN – 14 bit CCD camera with a resolution of 2048×2048 pixels [29]), using a 20.5 keV energy beam. From these four scans, two 3D images were reconstructed from the radiographs recorded at the two shorter distances, using the standard absorption mode (filtered back projection reconstruction) and a third one using the holotomographic mode (based on phase contrast). 3D holotomographic images were reconstructed by combining the four scans [30], using the specific algorithm proposed by Langer [31, 32]. Finally, these scans were performed for each loading level (50, 68, 74, 80, 86 and 92 N). In total, the entire experiment required 72 scans (3 fields of view \times 4 distances \times 6 loading levels) with each scan consisting of 1500 radiographs.

Due to the length of acquisition time for each scan (25 min), it was not possible to observe the entire gauge length of the specimen. However, a simple radiograph for the whole length was acquired at 92 N. Finally, another sample (called specimen #2) was loaded until failure (115 N) with the same tensile device. A radiograph of the whole

specimen was acquired after failure. To summarize, three distinct kinds of observation have been made:

- A. the 3D images of a 1.65 mm long region of the specimen #1 observed at six successive loading levels,
- B. the radiograph of the whole specimen #1 (about 14 mm long) under tensile loading at 92 N,
- C. the radiograph of the longest part of the broken specimen #2 (about 12 mm).

1.3. Damage detection

1.3.1. Matrix cracking (obs.A)

One goal of this study is to characterize the matrix crack morphology and its evolution with a load increase. Indeed, as presented in figure 3 (the detection procedure is detailed below), matrix cracks have a specific morphology which requires accurate locating. Such a result was obtained by spotting grey level variations in 3D images caused by the crack (figure 4). These variations could be visually noticed by routine observation of transverse slices of the tow. In the following, a “crack width” (along the axial direction) is defined from the number of transverse slices crossed by the crack (see figure 3). Note that crack openings cannot be characterized with accuracy because image resolution is not sufficient.

Moreover, the crack effects are more noticeable on the images reconstructed from the second distance radiographs than from the first. In fact, it is now well known that when a synchrotron source is used, an additional phase contrast due to diffraction effects appears on projections that improves the efficiency of damage detection [15, 33]. This contrast, invisible at the zero distance, is enhanced as the sample/detector distance increases. However, an increase in distance also emphasizes diffraction fringes on the

crack edges, making a quantitative observation of the crack more difficult. Although the crack is less noticeable on holotomographic reconstructions, diffraction fringes do not appear on these reconstructed images (figure 4) as the reconstruction procedure takes into account their physical origin [15, 30]. In order to precisely locate the crack within the section, a specific procedure was established to automatically detect the cracks in the volume by combining the three distinct reconstructions.

Considering a sub-volume containing a matrix crack (figure 1), the detection procedure is based on the processing of the grey level variation in the axial (Z) direction for all (X,Y) positions on the transverse plane. An example of such an evolution for a given (X,Y) position is provided in figure 5a. The crack leads to an important variation of the grey levels on a relatively short height among the three referenced reconstructions. The aim of the automatic procedure is to spot and locate this fluctuation in the axial direction, while reducing the detection of artifacts such as microstructure changes (matrix/pore interface) or image noise effects. Thus, a specific filter has been developed (figure 5b). It corresponds to the ratio of the norm of the grey level gradient along the Z-direction to the average derivative in a vicinity along Z (defined in figure 5a). In addition, the derivative was smoothed prior to the filtering in order to reduce the noise effect, using a centered moving average (10 voxels window along the Z-direction). A crack was then detected when the three global maxima (corresponding to the three reconstructions) of the filtered grey levels were separated by less than 10 voxels, ie 2.8 μm , which specifies the accuracy of the crack location. Otherwise, the material is considered healthy for the (X,Y) position and for all Z slices of the sub-volume. All (X,Y) positions are processed independently this way.

A combination of the three reconstructed volumes allows for reducing the detection of artifacts, like diffraction fringes at other interfaces. Moreover, the few number of detections located in the porous phase were removed.

Besides the main cracks that are detectable using the automatic procedure, there are small matrix cracking zones located on the periphery of the sample (isolated fiber group) or within the minicomposite. These are called minor cracks. They lead to a far smaller grey level variation along the Z axis, similar in intensity to image noise. As a result, the automatic detection procedure could not be used. However, because of their small size (about 5% of the global section) and their limited number, a manual axial location based on a direct observation of the images was sufficient to characterize them. The tomographic images resulting from observation A also show a few fiber failures which were easy to detect visually. Nevertheless, the observed field of view was far too small and the fiber breaking density too low to get statistically representative data about fiber breaking. Fiber/matrix debonding was not observable on these images.

1.3.2. Fiber breaking (obs.B and C)

In order to study fiber break distribution under load (92 N) and after failure, simple radiographs were useful to locate both fiber failures and main matrix cracks along the entire minicomposite length, as shown on figure 6a. While a few minor cracks were detected (they were harder to find on those images), they were not reported here. The detection was limited to visual observation leading to an inventory of fiber break and main matrix crack positions. Fiber crack openings and crack widths, as defined in section 1.3.1, can also be estimated (figure 6).

2. Results and discussion

2.1. Matrix cracking

2.1.1. Matrix crack distribution

The axial distribution of main matrix cracks and fiber breaks (as defined in section 1.3) are presented in figure 7 from radiograph observation performed at 92 N of the entire minicomposite (obs. B). At this loading, the matrix cracking can be assumed to be completed (see figure 2) so the average intercrack distance at saturation of crack number density was estimated to be equal to 250 μm . This value is consistent with crack spacing distances measured on similar minicomposites after classical tensile tests [3] (173 μm to 350 μm). The field of view of the tomography observations (obs. A) is also reported in figure 7. Before studying matrix crack morphology and propagation in detail, the evolution of the damage axial distribution was investigated by visual detection in the CT-reconstructions for the six different loading levels (figure 8). A first observation is that most cracks evolve when the load is increasing, in the sense that their width, as defined before, increases. Moreover, some of the minor cracks developed into main cracks, but the majority remained isolated.

The damage distribution is then compared with the effective section and surface porosity fraction variations in the axial direction (figure 8). The purpose is to study a potential link between damage location and these global characterizations of the microstructure. Both were estimated from a threshold of the holotomographic image.

The porosity of a section is here defined as the ratio of the closed pore area over the largest connex part of the composite section. Open pores on the periphery are not taken into account. These measurements are sensitive to the threshold choice. Its impact (relative error) was estimated at $\pm 2\%$ for the effective section and $\pm 10\%$ for the porosity fraction. The emphasis here is on the porosity variation along the minicomposite which

does not significantly depend on the threshold. Note also that the sharp porosity variations correspond to openings or closings of peripheral pores.

These observations did not evidence any clear link between crack locations and these global microstructure quantifications. Crack locations do generally not coincide with local extrema of effective section or porosity. Crack 2 is an exception, as it coincides with a local minimum of the effective section and thus a local maximum of average axial stress, but this is far from a general features.

2.1.2. Matrix crack propagation

The automatic procedure described in section 1.3 was used to detect the six main cracks, numbered in figure 8, for all of the six loading levels applied during observation A. Six sub-volumes, centered on the six main cracks observed at 92 N, were defined to compute the detection. Figure 9 describes the 3D geometry of the six detected cracks, in the form of the height Z of each crack as a function of the (X,Y) positions on the transverse plan. Only loading levels indicating crack propagation are presented (for example crack 2 did not propagate between 68 N and 74 N).

Two preliminary comments can be made before going into detail. Firstly, projections of cracks 1 and 6 are less clear than others. Contrast variations (like the one presented in figure 5) were far less pronounced for these two cracks. This is probably a consequence of a smaller crack opening. Secondly, the minor crack 3b presented in figure 10 and main crack 3a are complementary. As presented in figure 8, the two cracked zones were independent before the last loading step.

Concerning the crack morphology at 92 N, all six main cracks spread across the entire minicomposite section. They are not flat and typically follow a spiral shape around the fiber direction, except for crack 4 which presents an axial symmetry. Note also that the

crack elongation in the fiber direction – from 40 μm up to more than 100 μm – is quite large with respect to the intercrack distance (250 μm at saturation).

Pertaining to crack propagation, two or three distinct propagation states were observed depending on the crack. For example, cracks 2, 3, 4 and 6 propagation states followed three typical steps: crack initiation in a localized peripheral zone of the minicomposite, crack propagation on the entire periphery, and finally, propagation towards the section center. Crack 5 also initialized on the periphery, but the intermediate propagation state was not caught during observations. Lastly, although it was not revealed by the detection process, crack 1 initiation was visually detected and occurred inside the minicomposite section at 86 N.

Moreover, cracks 2, 3 and 4 did not propagate between 68 and 74 N. This revealed a discontinuous propagation. Furthermore, even if the matrix cracking saturation was supposed to be reached (ie no additional crack appears), the propagation was not achieved at 74 N. These results contradict the usual 1D modeling of minicomposite [6, 9], which assumes that the matrix cracks suddenly spread across the entire section with a uniform crack opening (ie propagation stage is ignored).

2.2. *Fiber breaking*

Radiographs resulting from observations B and C lead to statistical data about fiber breaking along the minicomposite under loading (92 N) and after failure. Following figure 7, fiber breaks appeared homogeneously along the minicomposite, mostly located in the vicinity of the matrix cracks. The fiber break density was rather low, with 4.8 broken fibers per mm (ie less than 1% fibers per mm).

Considering post-failure observations without counting final breaks (figure 11), approximately 220 fiber breaks were observed in the 12 mm long half minicomposite.

The break density is far less homogeneous (figure 12). In fact, most fiber breaks are located within 2 mm of the failure zone. On the other hand, the fiber break distribution is quite homogeneous at other locations. It has a density of approximately 5 breaks per mm (calculated on region III in figure 12), very similar to the density at 92 N.

Additionally, observation A shows that the first fiber breaks observed with 3D tomography appeared at 80 N (figure 8). This load matches the final stage of matrix crack propagation inside the minicomposite.

To summarize, it appears that fiber breaking occurs at the completion of matrix cracking propagation with a rather low density and a uniform distribution with preferred locations near matrix cracks. At the load resulting in ultimate failure, fiber breaking was centralized within an area (about 4 mm long) surrounding the ultimate failure location. Finally, fiber crack openings reported on figure 12 are 7 μm long in average far from the failure zone. Fiber breaks located near the failure zone exhibit larger openings (up to 50 μm).

In agreement with these observations, two different scenarios could be proposed. On the one hand, a random uniform fiber breaking develops slowly as the stress increases and the localization of the fiber density observed on figure 12 is the consequence of dynamic effects during failure. On the other hand, the random fiber breaking starts with a uniform distribution, then a localization of the break density occurs and leads to the ultimate failure. This second scenario is in better agreement with the final slight non-linearity observed on macroscopic curves, but additional experiments are required to

conclude. However, in both cases, this characterization shows that one fiber can fail twice along the minicomposite. This has also been observed on a fiber in obs.A.

These experimental results are inconsistent with the assumption of the classical fiber bundle model [34] used in some 1D models [6, 35] which supposes that once broken, a fiber does not participate anymore to the load transfer throughout the whole composite (and as a consequence breaks only once). Fiber break observations are rather in line with works which take into account a sliding length around a break necessary for the fiber to recover back its previously carried stress [36, 37, 11]. Moreover, those works also emphasize a localization region around some plane weaker than the others along the composite where fiber breakage will continue once final breakdown occurs there [38, 39, 40].

3. Concluding remarks

Standard 2D techniques are not sufficient to characterize damage mechanisms such as matrix crack propagation and fiber breaking occurring within the material. Therefore, an in-situ tensile test was performed on a SiCf/SiC minicomposite under X-ray microtomography to observe damage evolution. The matrix crack detection required the use of a high resolution equipment available through synchrotron radiation at the ESRF. Two observation techniques were used and resulted in the following damage characterization:

- The tomography (absorption and holotomographic mode) performed on a minicomposite at 6 successive loading levels was necessary to observe matrix crack evolutions within the sample. A few fiber breaks may also be observed.
- Simple radiograph acquisition was much faster than tomography acquisition.

Therefore, the whole minicomposite observations could be performed under loading and

after failure. Matrix crack and fiber break characterizations are limited to their spatial location along the sample, but it continues to be a useful way to get statistical data about fiber breaking. Moreover, the resolution was sufficient to estimate fiber break openings. These observations provided a deeper insight on damage mechanisms:

- Besides well known transverse cracks and fiber breaks, 3D images revealed minor matrix cracks. These small matrix cracking zones located within the minicomposite could become a transverse crack or could remain localized. However, the cracked sections are so small that the influence on the macroscopic damageable behavior is likely to be insignificant compared to main cracks.
- A specific automatic procedure was developed to detect and locate main cracks along the minicomposite. Most of them are not flat but typically follow a spiral shape which is quite elongated in the fiber direction. In addition, the matrix crack propagates slowly and discontinuously within the bundle of fibers, even after the cracking saturation. They mostly appear at first on the peripheral zone, and then propagate towards the center of the section. This experimental evidence is contrary to common assumption of 1D models which ignore crack propagation. Such assumptions that are appropriate for microcomposites (containing a single fiber) [10], may be insufficient for minicomposites.
- Fiber breaking seems to begin immediately after matrix crack propagation ends. Fibers fail, at first homogeneously, and are typically located in the vicinity of matrix cracks. Fiber break density stabilizes around 5 fiber failures per mm, except in a short zone (a few millimeters) surrounding the ultimate failure where the break number density is much greater. Fiber openings are also much larger in this area. Two scenarios have been proposed to explain these observations, involving dynamic effects induced by the

ultimate failure or fiber breaking localization leading to the ultimate failure. Moreover, experimental results suggest selecting models based on frictional load-sharing rather than neglecting the contribution of broken fibers to the load transfer.

Acknowledgement

The authors are very grateful to M.Langer for his help in reconstructing holotomographic images. The ID19 team is also acknowledged for its help during the experiment at the ESRF.

References

- [1] G. N. Morscher, Tensile stress rupture of SiCf/SiCm minicomposites with carbon and boron nitride interphases at elevated temperatures in air, *Journal Of The American Ceramic Society* 80 (8) (1997) 2029–2042.
- [2] S. Bertrand, R. Paillet, J. Lamon, SiC/SiC minicomposites with nanoscale multilayered fibre coatings, *Composites Science And Technology* 61 (3) (2001) 363–367.
- [3] C. Sauder, A. Brusson, J. Lamon, Influence of interface characteristics on the mechanical properties of Hi-Nicalon type-S or Tyranno-SA3 fiber-reinforced SiC/SiC minicomposites, *International Journal Of Applied Ceramic Technology* 7 (3) (2010) 291–303.
- [4] C. Baxevanakis, D. Jeulin, J. Renard, Fracture statistics of a unidirectional composite, *International Journal Of Fracture* 73 (2) (1995) 149–181.
- [5] C. Y. Hui, S. L. Phoenix, M. Ibnabdeljalil, R. L. Smith, An exact closed-form solution for fragmentation of weibull fibers in a single filament composite with applications to fiber-reinforced ceramics, *Journal Of The Mechanics And Physics Of Solids* 43 (10) (1995) 1551–1585.
- [6] N. Lissart, J. Lamon, Damage and failure in ceramic matrix minicomposites: Experimental study and model, *Acta Materialia* 45 (3) (1997) 1025–1044.
- [7] A. T. DiBenedetto, M. R. Gurvich, Statistical simulation of fiber fragmentation in a single-fiber composite, *Composites Science And Technology* 57 (5) (1997) 543–555.

- [8] W. A. Curtin, B. K. Ahn, N. Takeda, Modeling brittle and tough stress-strain behavior in unidirectional ceramic matrix composites, *Acta Materialia* 46 (10) (1998) 3409–3420.
- [9] J. Lamon, Stochastic approach to multiple cracking in composite systems based on the extreme-values theory, *Composites Science And Technology* 69 (10) (2009) 1607–1614.
- [10] E. Castelier, L. Gélébart, C. Lacour, C. Lantuéjoul, Three consistent approaches of the multiple cracking process in 1D composites, *Composites Science and Technology* 70 (15) (2010) 2146–2153.
- [11] S. L. Phoenix, Statistical issues in the fracture of brittle-matrix fibrous composites, *Composites Science and Technology* 48 (1-4) (1993) 65–80.
- [12] S. Bertrand, P. Forio, R. Pailler, J. Lamon, Hi-Nicalon/SiC minicomposites with (pyrocarbon/SiC)(n) nanoscale multilayered interphases, *Journal Of The American Ceramic Society* 82 (9) (1999) 2465–2473.
- [13] J. Martinez-Fernandez, G. N. Morscher, Room and elevated temperature tensile properties of single tow Hi-Nicalon, carbon interphase, CVI SiC matrix minicomposites, *Journal Of The European Ceramic Society* 20 (14-15) (2000) 2627–2636.
- [14] S. R. Stock, Recent advances in X-ray microtomography applied to materials, *International Materials Reviews* 53 (3) (2008) 129–181.
- [15] J. Y. Buffière, E. Ferrière, H. Proudhon, W. Ludwig, Three-dimensional visualisation of fatigue cracks in metals using high resolution synchrotron X-ray micro-tomography, *Materials Science And Technology* 22 (9) (2006) 1019–1024.
- [16] S. A. McDonald, M. Preuss, E. Maire, J. Y. Buffière, P. M. Mummery, P. J. Withers, X-ray tomographic imaging of Ti/SiC composites, *Journal Of Microscopy-Oxford* 209 (2003) 102–112.
- [17] T. M. Breunig, J. H. Kinney, S. R. Stock, MicroCT (microtomography) quantification of microstructure related to macroscopic behaviour - Part 2 - Damage in SiC-Al monofilament composites tested in monotonic tension and fatigue, *Materials Science And Technology* 22 (9) (2006) 1059–1067.

- [18] Y. C. Hung, J. A. Bennett, F. A. Garcia-Pastor, M. Di Michiel, J. Y. Buffière, T. J. A. Doel, P. Bowen, P. J. Withers, Fatigue crack growth and load redistribution in Ti/SiC composites observed in situ, *Acta Materialia* 57 (2) (2009) 590–599.
- [19] P. J. Schilling, B. P. R. Karedla, A. K. Tatiparthi, M. A. Verges, P. D. Herrington, X-ray computed microtomography of internal damage in fiber reinforced polymer matrix composites, *Composites Science And Technology* 65 (14) (2005) 2071–2078.
- [20] D. R. B. Aroush, E. Maire, C. Gauthier, S. Youssef, P. Cloetens, H. D. Wagner, A study of fracture of unidirectional composites using in situ high-resolution synchrotron X-ray microtomography, *Composites Science And Technology* 66 (10) (2006) 1348–1353.
- [21] A. J. Moffat, P. Wright, J. Y. Buffière, I. Sinclair, S. M. Spearing, Micromechanisms of damage in 0 degrees splits in a [90/0](s) composite material using synchrotron radiation computed tomography, *Scripta Materialia* 59 (10) (2008) 1043–1046.
- [22] A. Guvenilir, T. M. Breunig, J. H. Kinney, S. R. Stock, New direct observations of crack closure processes in Al-Li 2090 T8E41, *Philosophical Transactions Of The Royal Society Of London Series A-Mathematical Physical And Engineering Sciences* 357 (1761) (1999) 2755–2775.
- [23] E. Ferrié, J. Y. Buffière, W. Ludwig, A. Gravouil, L. Edwards, Fatigue crack propagation: In situ visualization using X-ray microtomography and 3D simulation using the extended finite element method, *Acta Materialia* 54 (4) (2006) 1111–1122.
- [24] B. Muller, F. Pfrunder, L. Chiocca, N. D. Ruse, F. Beckmann, Visualising complex morphology of fatigue cracks in voxel based 3D datasets, *Materials Science And Technology* 22 (9) (2006) 1038–1044.
- [25] S. B. Lee, S. R. Stock, M. D. Butts, T. L. Starr, T. M. Breunig, J. H. Kinney, Pore geometry in woven fiber structures: 0 degrees/90 degrees plain-weave cloth layup preform, *Journal Of Materials Research* 13 (5) (1998) 1209–1217.
- [26] A. Morales-Rodriguez, P. Reynaud, G. Fantozzi, J. Adrien, E. Maire, Porosity analysis of long-fiber-reinforced ceramic matrix composites using X-ray tomography, *Scripta Materialia* 60 (6) (2009) 388–390.
- [27] L. Gélébart, C. Chateau, M. Bornert, J. Crépin, E. Boller, X-ray tomographic characterization of the macroscopic porosity of chemical vapor infiltration SiC/SiC

composites: Effects on the elastic behavior, *International Journal Of Applied Ceramic Technology* 7 (3) (2010) 348–360.

[28] L. Salvo, P. Cloetens, E. Maire, S. Zabler, J. J. Blandin, J. Y. Buffière, W. Ludwig, E. Boller, D. Bellet, C. Josserond, X-ray micro-tomography an attractive characterisation technique in materials science, *Nuclear Instruments & Methods In Physics Research Section B-Beam Interactions With Materials And Atoms* 200 (2003) 273–286.

[29] J. C. Labiche, O. Mathon, S. Pascarelli, M. A. Newton, G. G. Ferre, C. Curfs, G. Vaughan, A. Homs, D. F. Carreiras, The fast readout low noise camera as a versatile X-ray detector for time resolved dispersive extended X-ray absorption fine structure and diffraction studies of dynamic problems in materials science, chemistry, and catalysis, *Review Of Scientific Instruments* 78 (9) (2007) 091301.

[30] P. Cloetens, W. Ludwig, J. Baruchel, D. Van Dyck, J. Van Landuyt, J. P. Guigay, M. Schlenker, Holotomography: Quantitative phase tomography with micrometer resolution using hard synchrotron radiation X rays, *Applied Physics Letters* 75 (19) (1999) 2912–2914.

[31] M. Langer, P. Cloetens, J. P. Guigay, F. Peyrin, Quantitative comparison of direct phase retrieval algorithms in in-line phase tomography, *Medical Physics* 35 (10) (2008) 4556–4566.

[32] M. Langer, P. Cloetens, F. Peyrin, Regularization of phase retrieval with phase-attenuation duality prior for 3-D holotomography, *IEEE Transactions on Image Processing* 19 (9) (2010) 2428–2436.

[33] P. Cloetens, M. Pateyron-Salomé, J. Y. Buffière, G. Peix, J. Baruchel, F. Peyrin, M. Schlenker, Observation of microstructure and damage in materials by phase sensitive radiography and tomography, *Journal Of Applied Physics* 81 (9) (1997) 5878–5886.

[34] H. E. Daniels, The statistical theory of the strength of bundles of threads .1., *Proceedings of the Royal Society of London Series A-mathematical and Physical Sciences* 183 (995) (1945) 405–435.

[35] J. Lamon, A micromechanics-based approach to the mechanical behavior of brittle-matrix composites, *Composites Science And Technology* 61 (15) (2001) 2259–2272.

- [36] W. A. Curtin, Theory of mechanical-properties of ceramic-matrix composites, *Journal of the American Ceramic Society* 74 (11) (1991) 2837–2845.
- [37] S. L. Phoenix, R. Raj, Scalings in fracture probabilities for a brittle matrix fiber composite, *Acta Metallurgica Et Materialia* 40 (11) (1992) 2813–2828.
- [38] W. A. Curtin, Fiber pull-out and strain localization in ceramic matrix composites, *Journal of the Mechanics and Physics of Solids* 41 (1) (1993) 35–53.
- [39] W. A. Curtin, The tough to brittle transition in brittle matrix composites, *Journal of the Mechanics and Physics of Solids* 41 (2) (1993) 217–245.
- [40] S. L. Phoenix, M. Ibnabdeljalil, C. Y. Hui, Size effects in the distribution for strength of brittle matrix fibrous composites, *International Journal of Solids and Structures* 34 (5) (1997) 545–568.

Figure captions

Figure 1: SEM micrographs of (a) minicomposite polished cross section; (b) cracked minicomposite under tension (75 N), arrows point out matrix cracks.

Figure 2: Macroscopic tensile behavior obtained with a macroscopic device. The loading levels at which the tensile test was interrupted for the μ -CT observations are also reported.

Figure 3: (a) Sub-volume containing a matrix crack; (b-c) Detected matrix crack from two different angles of view.

Figure 4: Reconstruction of a transverse slice in absorption contrast (first two distances) and holotomographic mode within a matrix crack.

Figure 5: Filtering of grey levels : (a) grey level evolution in the fiber direction through a matrix crack; (b) filtering results.

Figure 6: (a) Radiograph of the minicomposite at a tensile load of 92 N (b) Zoom on a fiber break.

Figure 7: Damage location along the entire minicomposite at 92 N as detected from the radiographs (obs. B). Blue line widths are directly related to crack widths. The minicomposite part focused on by observation A is framed with a dashed line.

Figure 8: Damage location along the minicomposite in the area observed by tomography for the 6 successive loading levels (obs. A) compared to the variations of the effective section (fibers and matrix, without porosity) and the surface porosity fraction. Triangular markers point out peripheral pore openings or closings.

Figure 9: Results of main crack detections (projections onto the transverse plane). Color scale corresponds to the local height of each cracked voxel (with respect to the lower face of each sub-volume). Note that scale is different for each crack.

Figure 10: Projection onto the transverse plane of crack 3b, which is an extension of the main crack 3a.

Figure 11: Radiographs after failure located near (I.) and far from the ultimate failure zone (II.) (see figure 12). Fiber breaks are highlighted.

Figure 12: Fiber break local density and opening as a function of the distance to the ultimate failure zone. The local density was computed over a 1 mm moving window.

Regions I. and II. designate radiograph locations presented in figure 11. Region III. is the minicomposite part far from the failure zone when crack density appears uniform.

Figure 1

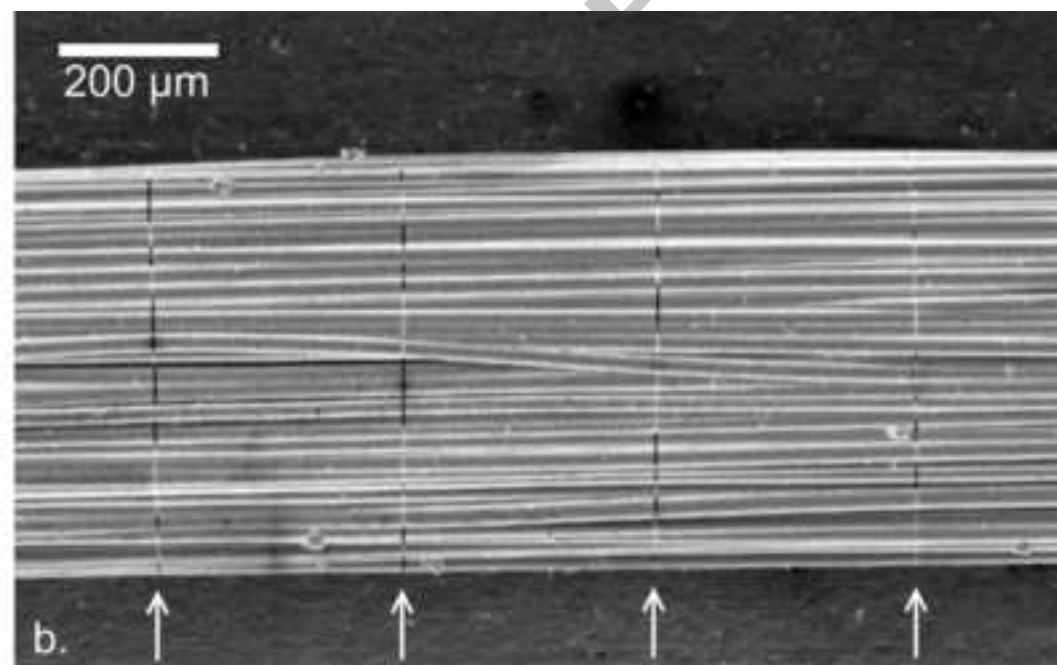
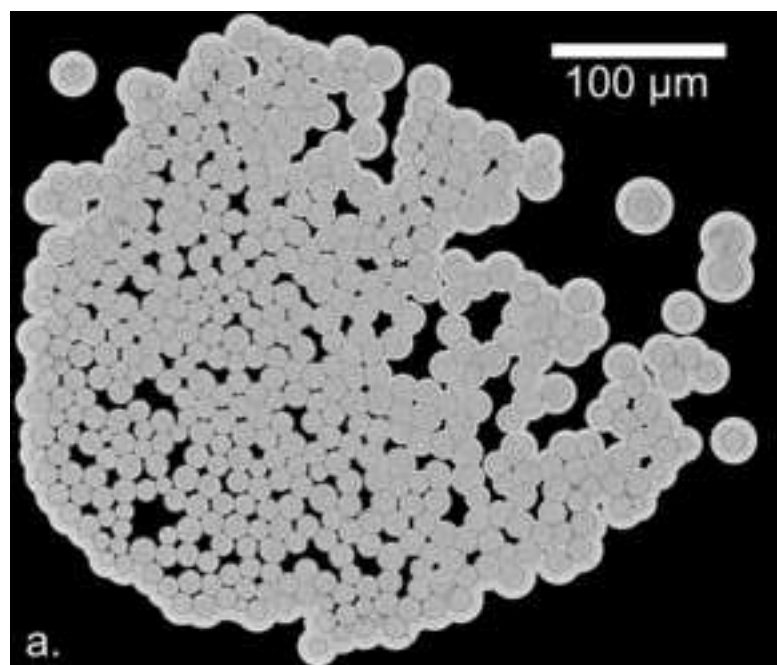
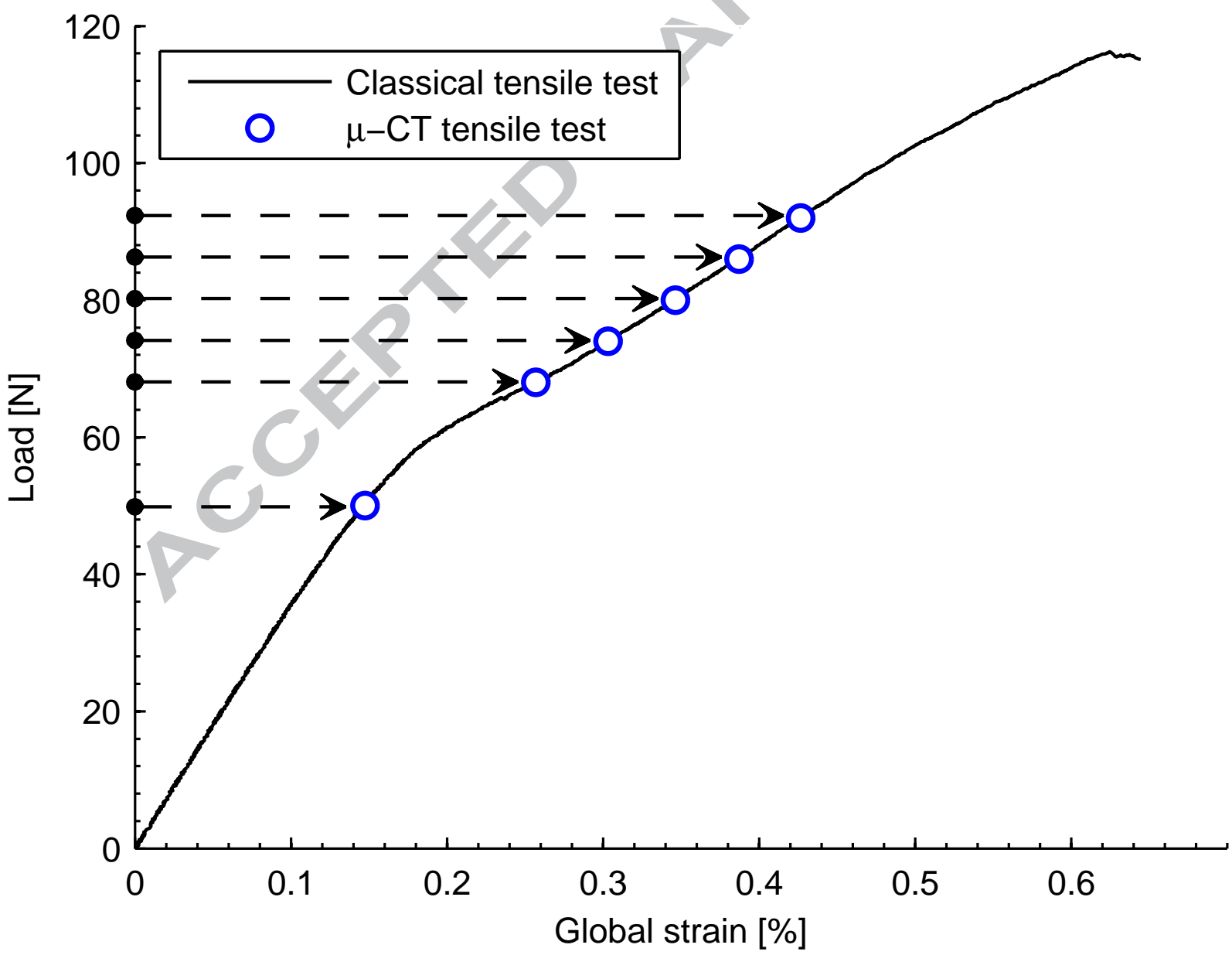


Figure 2



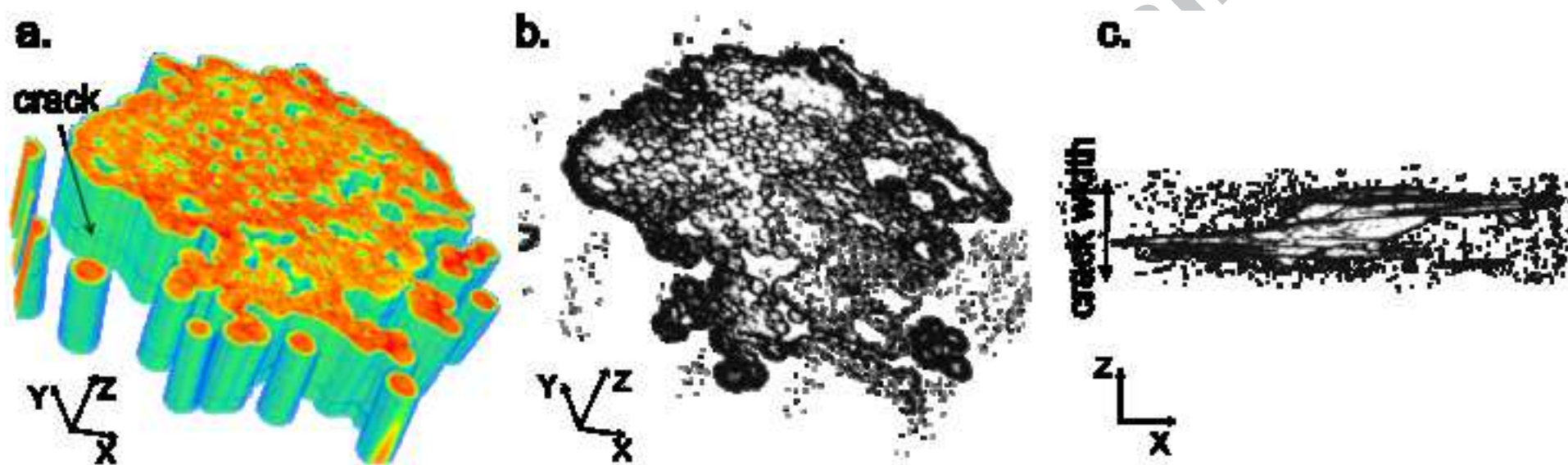


Figure 4

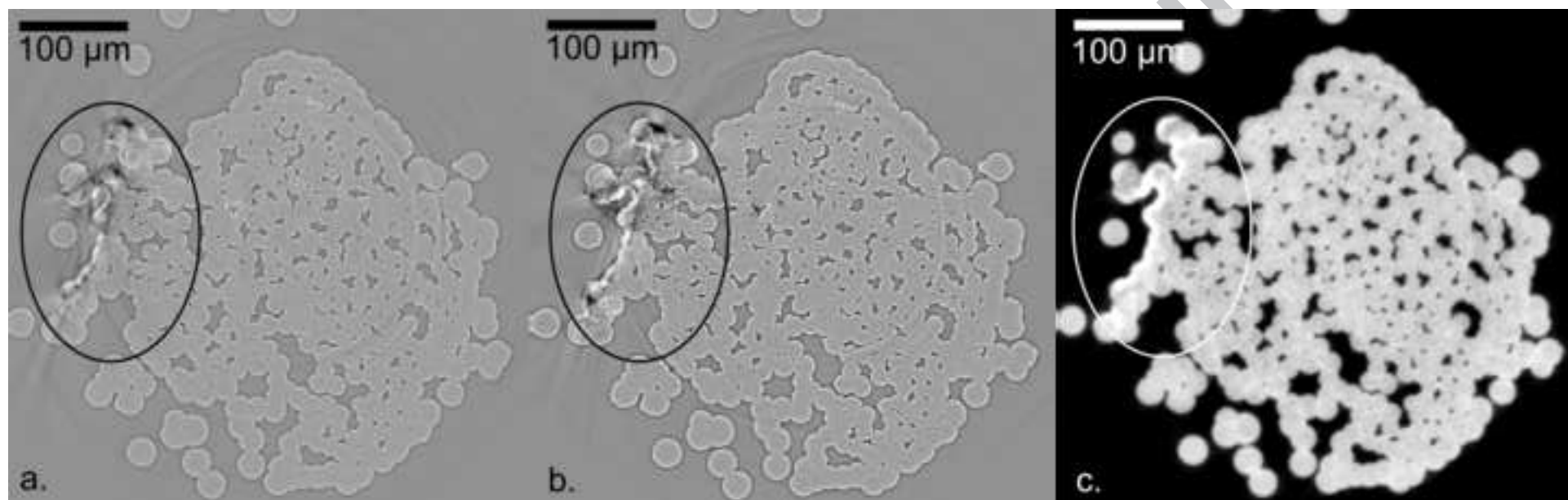


Figure 5

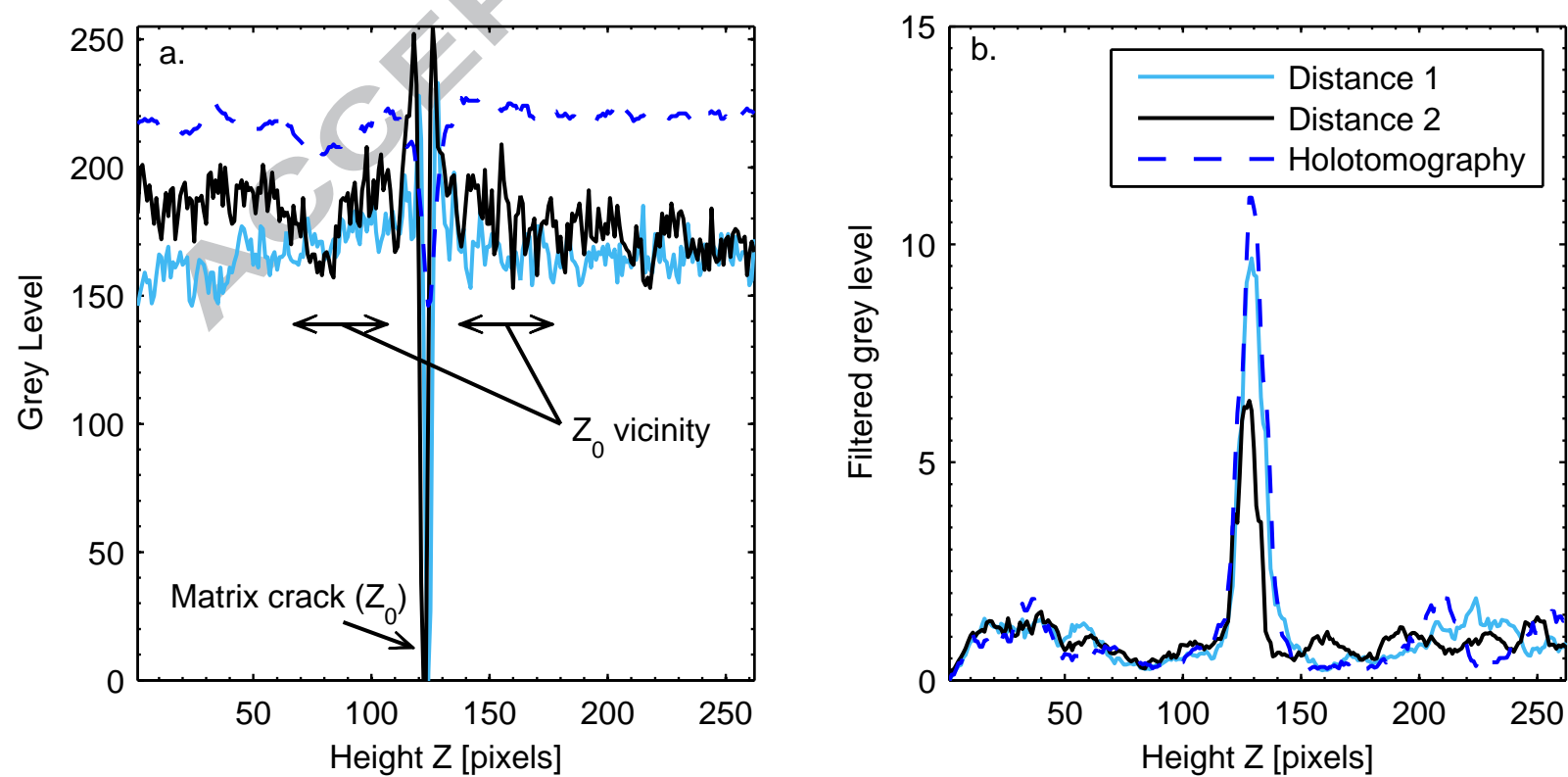


Figure 6

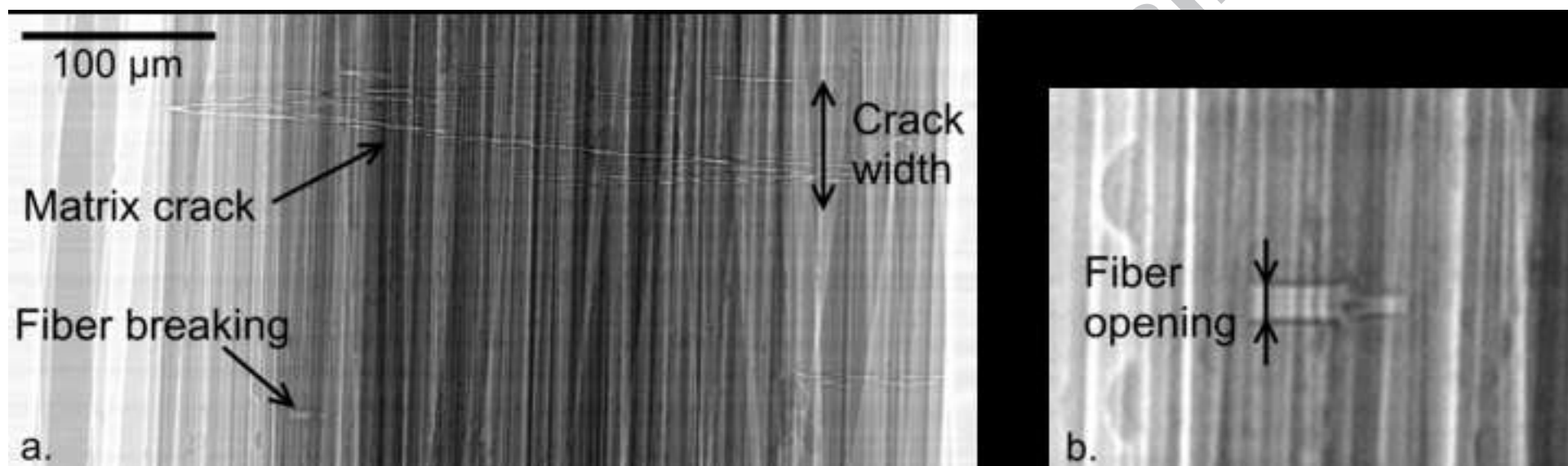


Figure 7

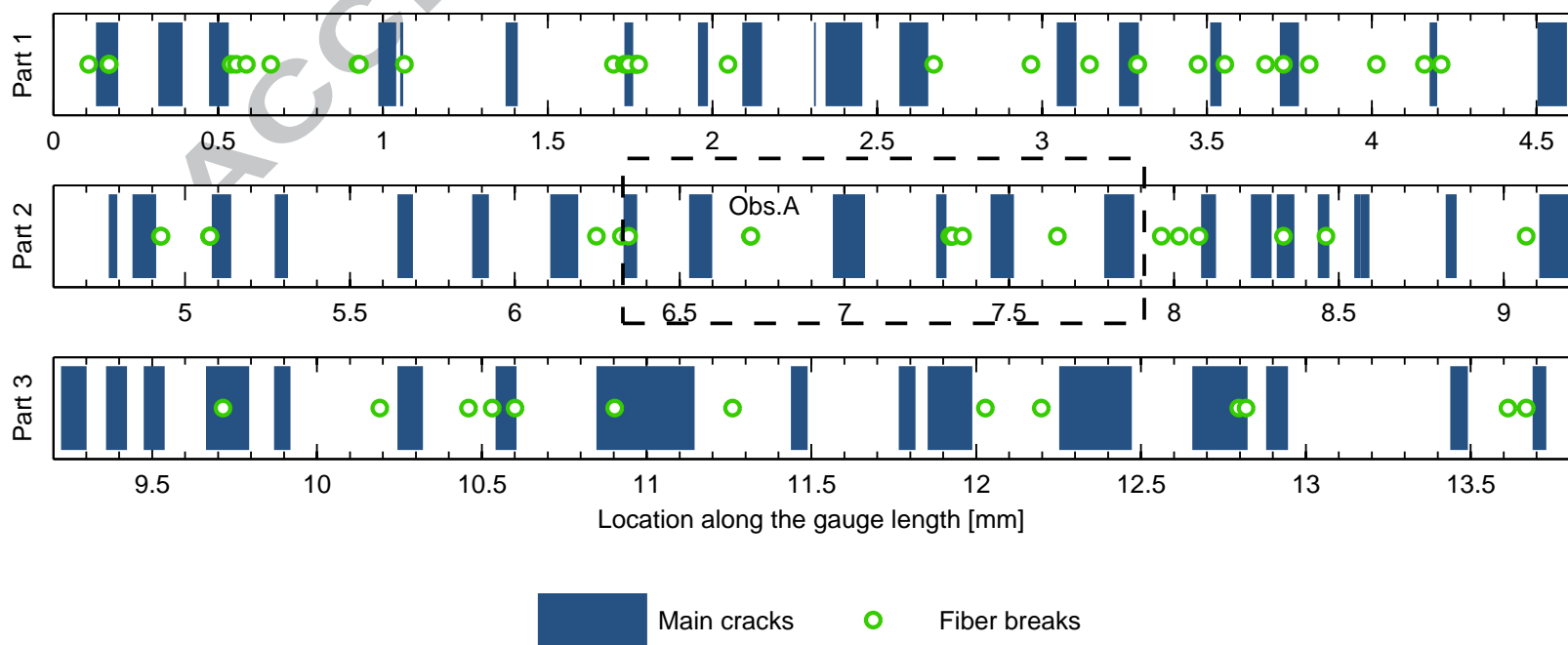


Figure 8

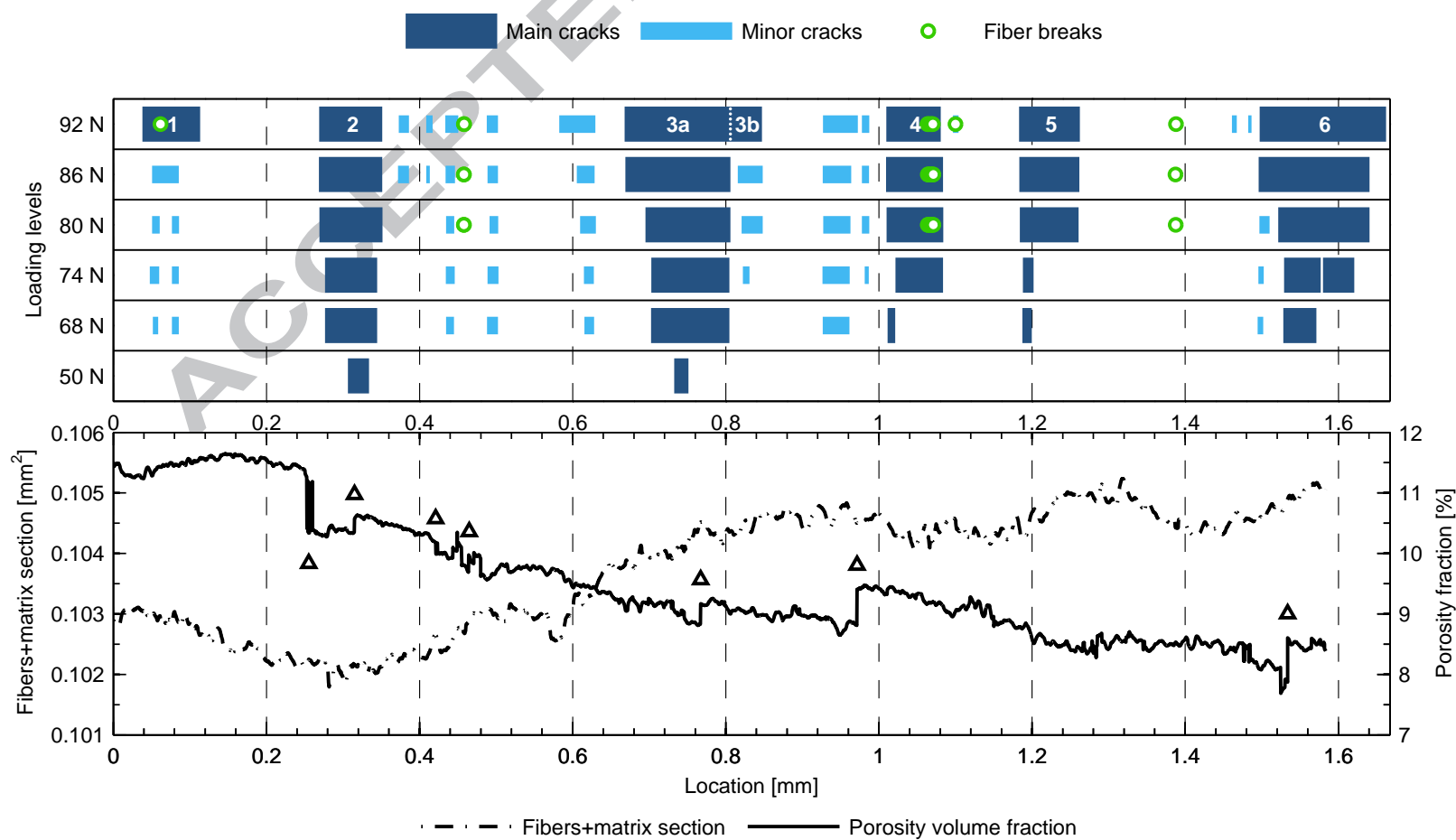


Figure 9 - color

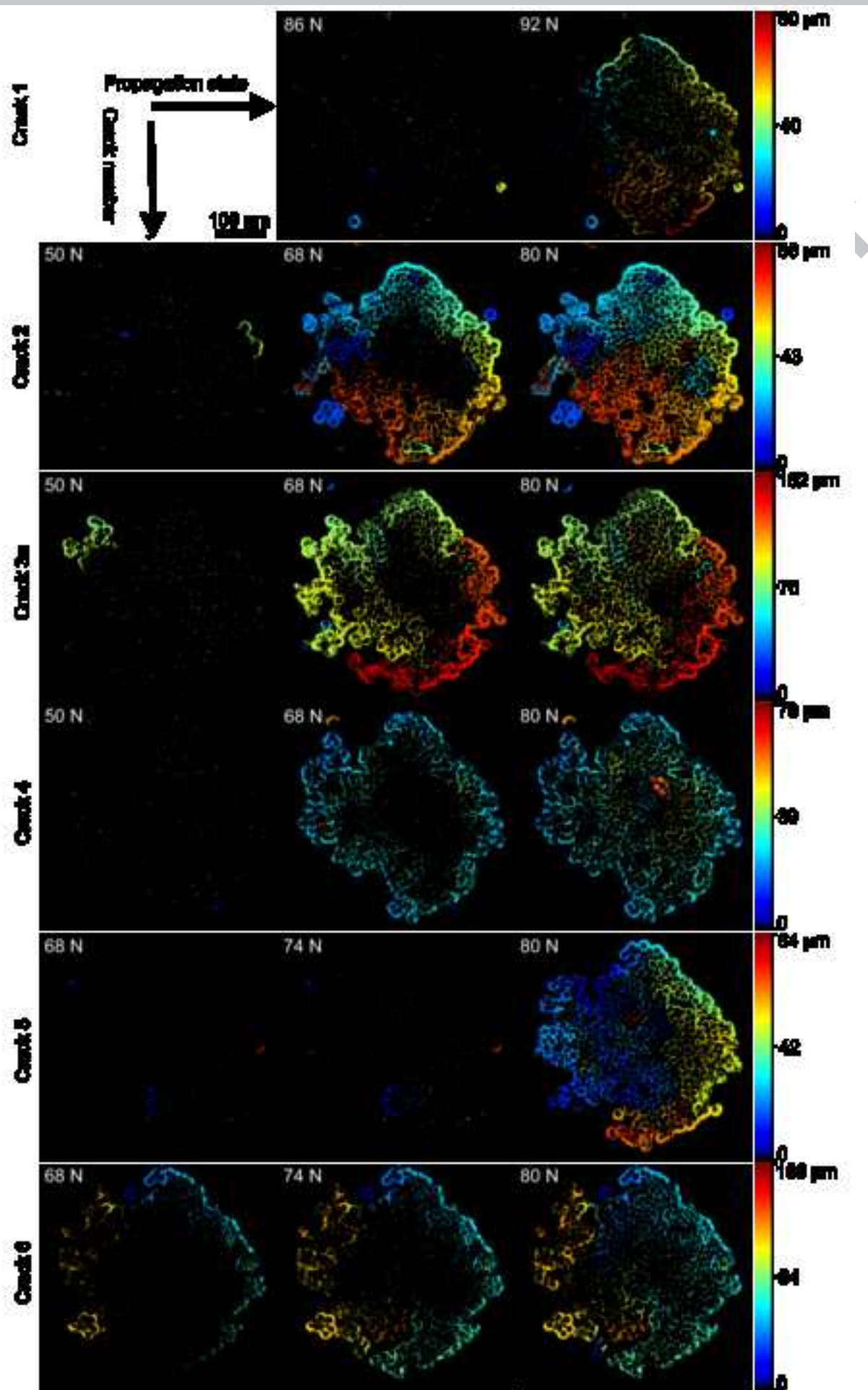


Figure 10 - color

ACCEPTED MANUSCRIPT

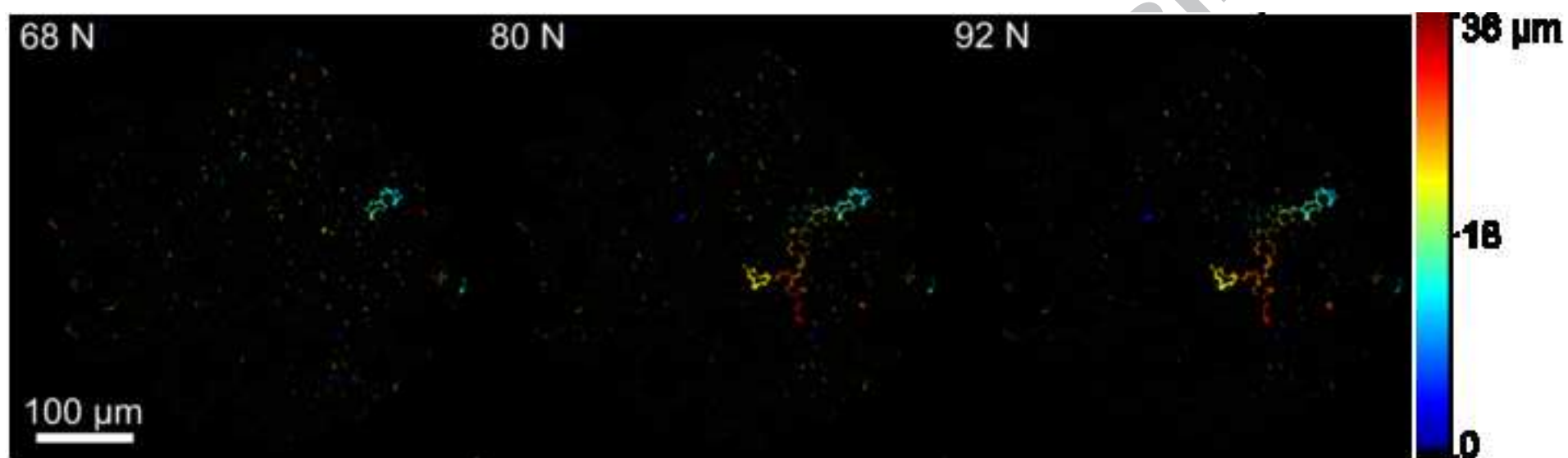


Figure 11

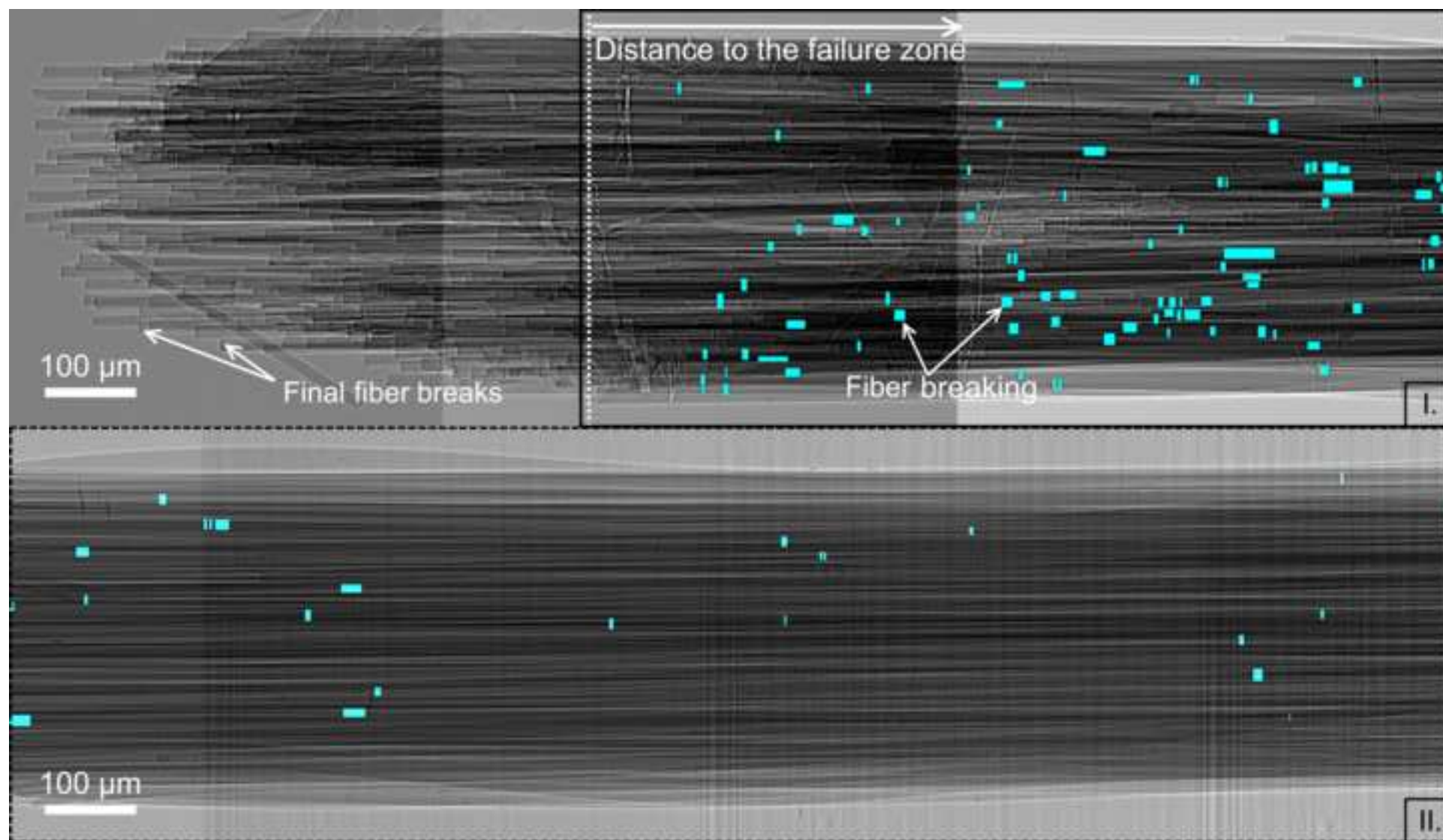


Figure 12

